THE JOURNAL OF
PHYSICAL
CHEMISTRY
A

VOLUME 108, NUMBER 20, MAY 20, 2004

FEATURE ARTICLE

Isothermal Nucleation Rates in Supersonic Nozzles and the Properties of Small Water Clusters

Yoo Jeong Kim,[†] Barbara E. Wyslouzil,*[,†,||] Gerald Wilemski,[‡] Judith Wölk,[§] and Reinhard Strey[§]

Department of Chemical Engineering, Worcester Polytechnic Institute, Worcester, Massachusetts 01609-2280, Department of Chemical Engineering, The Ohio State University, Columbus, Ohio 43210-1180, Department of Physics, University of Missouri—Rolla, Rolla, Missouri 65409-0640, and Institut für Physikalische Chemie, Universität zu Köln, 50939 Köln, Germany

Received: October 8, 2003; In Final Form: February 10, 2004

We make direct measurements of stationary, homogeneous nucleation rates, $J = N/\Delta t$, in supersonic Laval nozzles. We determine the number densities, N, of droplets formed from small-angle neutron scattering (SANS) experiments and the time intervals during which nucleation occurs, $\Delta t \approx 10\ \mu$s, from static pressure measurements along the axis of the nozzle. Applying these techniques to nozzles with different expansion rates, we obtain the first isothermal nucleation rate measurements as a function of supersaturation for these devices with a relatively small error margin in J of ±50%. At temperatures T of 210, 220, and 230 K, the maximum nucleation rates for D_2O lie in the range $4 \times 10^{16} < J/\text{cm}^{-3}\text{s}^{-1} < 3 \times 10^{17}$ for supersaturations S ranging from 46 to 143. At the highest temperature, the predictions of classical nucleation theory lie slightly below the experimental points but are still within experimental error. At the lower temperatures, the classical predictions lie well below the measured values. The discrepancy increases as the temperature is lowered and exceeds the measurement error bars. In contrast, the predictions of the empirical temperature correction function to the classical theory proposed by Wölk and Strey (Wölk, J.; Strey, R. *J. Phys. Chem. B* **2001**, *105*, 11683) agree quite well with the experimental data points over the entire supersaturation and temperature ranges. Finally, we apply the first and second nucleation theorems to the data and directly estimate the number of molecules in the critical cluster n^* and the excess internal energy $E_x(n^*)$, respectively. The agreement between these values and the classical values predicted assuming that the critical cluster is a compact spherical object is really quite good even though under our conditions n^* is less than 10. The good agreement for the classical values of the excess internal energy implies that the poor temperature dependence of the classical rate predictions arises from the classical theory's failure to treat correctly the excess internal entropy of the critical cluster.

I. Introduction

First-order phase transitions such as crystallization, condensation, melting, and evaporation are found not only in industrial processes but also in daily life. The macroscopic phase transition is initiated by nucleation—the formation of the first fragments of the new phase—and is followed by growth and, finally, by aging. Of these three processes, nucleation is still the least well understood, the hardest to predict, and the hardest to measure. A closer examination of nucleation is important because it helps us understand the kinetics of phase transitions and develop better models of processes where phase transitions occur. Our particular concern is homogeneous nucleation, where the phase transition occurs in the absence of any nucleation centers. We

---

* Corresponding author. E-mail: wyslouzil.1@osu.edu.
[†] Worcester Polytechnic Institute.
[‡] University of Missouri—Rolla.
[§] Universität zu Köln.
[||] The Ohio State University.

10.1021/jp037030j CCC: $27.50

focus on the vapor-to-liquid phase transition of a single compound in excess carrier gas because this is one of the most well defined and extensively investigated systems available.[1,2] Devices used to investigate vapor-phase nucleation include thermal diffusion cloud chambers,[3−5] laminar flow tube reactors,[6−8] expansion cloud chambers,[9] shock tubes,[10,11] nucleation pulse chambers,[12,13] and supersonic nozzles.[14−24] Most of these devices are now capable of measuring nucleation rates as a function of temperature and supersaturation over 3 to 4 orders of magnitude.

Investigations of nucleation in supersonic nozzles began over 50 years ago[14−20] with the pioneering work of Oswatitsch.[14,21] Most experiments measured either the conditions at the onset of condensation or the correction factors to classical nucleation theory required to bring the model predictions into agreement with the experimental results. Recently, in Streletzky et al.,[22] we showed that we can derive peak nucleation rates $J_{\max}$ as a function of temperature and supersaturation in a shaped supersonic nozzle designed to decouple nucleation from droplet growth. We conducted small-angle neutron scattering (SANS) experiments to determine the aerosol number density and estimated the characteristic time associated with the nucleation process from the pressure profile measurements. In Khan et al.,[23] we extended these results and demonstrated that we could also acquire nucleation rates in a conventional Laval nozzle even though nucleation and growth are strongly coupled. We used the same approach in Heath et al.[24] to extract D_2O-H_2O binary nucleation rates. In Khan et al.,[23] we found that $J_{\max}$ was almost constant regardless of the initial temperature, the position of onset in the nozzle, the supersaturation, or the temperature corresponding to the maximum nucleation rate. Because one cannot significantly change the peak nucleation rate in a nozzle with a fixed expansion rate by modifying the operating conditions, one must work with a series of nozzles characterized by different expansion rates in order to observe a range of peak nucleation rates.

Most supersonic nozzle research has focused on water because water is important in industrial applications such as flows in steam turbines and around supersonic aircraft. Unfortunately, for the aerosol SANS measurements that are required to determine the aerosol number densities accurately, water poses difficulties because its low coherent scattering length density, $\Delta\rho = -0.56 \times 10^{10}$ cm^{-2}, combined with the low volume fraction of the sample, $\phi \approx 10^{-6}$, means that the SANS scattering signals are very weak. Heavy water (D_2O), in contrast, has a scattering length density of $\Delta\rho = 6.36 \times 10^{10}$ cm^{-2} and yields acceptable SANS spectra. Although light and heavy water have significantly different nucleation rates at a fixed vapor pressure,[13,24] the rates agree within experimental error when plotted as a function of the supersaturation. Thus, even though the thermophysical properties of the two isotopes differ, we can learn about the nucleation behavior of one isotope by studying the behavior of the other.

Our present objective is to build on our efforts in Khan et al.[23] and to measure isothermal nucleation rates of D_2O as a function of supersaturation in three conventional Laval nozzles. In addition to expanding the nucleation rate database for water, we want to obtain the number of molecules in the critical cluster, n^*, and the excess internal energy of the critical cluster, $E_x(n^*)$, for critical clusters containing fewer than 10 molecules. These quantities are derived from the measured nucleation rates by applying the first[25−27]

$$\left(\frac{\mathrm{d}(\ln J)}{\mathrm{d}(\ln S)}\right)_T \cong n^* \tag{1}$$

and second[28−29]

$$\left(\frac{\mathrm{d}(\ln J)}{\mathrm{d}T}\right)_{\ln S} \cong \frac{1}{kT^2}[L - kT + E_x(n^*)] \tag{2}$$

nucleation theorems, respectively. In eqs 1 and 2, J is the nucleation rate, S is the supersaturation, T is the temperature, k is the Boltzmann constant, and L is the latent heat of vaporization for the bulk liquid.

We start with the nozzle we used in Khan et al.[23] and then study two additional nozzles, one with a faster and the other with a slower expansion rate. We characterize condensation in all three nozzles for both isotopes of water, but almost all of our SANS measurements are made with D_2O. We chose target temperatures of 230, 220, and 210 K in order to compare the new results with our earlier measurements in Khan et al.[23] as well as with those of Wölk and Strey[13] and Mikheev et al.[8] that are 8−10 orders of magnitude lower. To compare the three data sets, we use the empirical function for homogeneous nucleation rates of water developed by Wölk and Strey.[13] Finally, we extract and compare the values of n^* and $E_x(n^*)$ for the three data sets.

II. Experiment

A. Materials and Physical Properties. We conducted condensation experiments using both H_2O and D_2O. The H_2O was deionized with a resistivity greater than 15 MΩ·cm and is assumed to have the natural distribution of H and D. The D_2O (DLM-4, Cambridge Isotope Labs, Andover, MA) had more than 99.9% D substitution. The thermophysical properties used to calculate the nucleation rates and to determine the other state variables of the flow (temperature, density, velocity, and condensate mass fraction) from the pressure measurements are the same as those we reported earlier.[13,24,30]

B. Supersonic Nozzles and Flow Apparatus. Figure 1 illustrates the setup for the current experiments. The main difference between these experiments and our earlier studies[23,24,30,31] is that all of the N_2 carrier gas is now drawn from the gas side of two high-pressure (∼250 kPa) liquid-nitrogen Dewars. In-line heaters (McIlrath's Automatic Electric Heater, Calco Controls Inc., Cary, IL, 1000 W) warm the gas and prevent the lines and regulators from freezing. One Dewar supplies up to ∼80% of the total N_2 flow, and a second Dewar provides the gas to disperse and vaporize the condensable liquid that is fed to the vaporizer using a peristaltic pump. Each liquid N_2 Dewar sits on a 500-kg balance, and the weight change is monitored by the data acquisition system in order to determine the mass flow rate of nitrogen. The mass flow rate of the condensable is measured in a similar manner.

In the plenum, the stagnation temperature T_0 is controlled by the water bath, and the stagnation pressure p_0 is controlled by adjusting the pressure regulator on the first N_2 Dewar. The static pressure p in the nozzle is measured as a function of position using a 1.27-mm o.d. stainless steel probe (i.d. = 0.97 mm, 61 cm long). The probe is sealed at the tip and has three 0.5-mm holes located 15 cm from the tip and evenly distributed around the circumference. The data acquisition system records the values of p_0, T_0, p, the weights of the Dewars, and the relative humidity of the gas stream entering the plenum.

For these studies, we used three conventional Laval nozzles. The first, nozzle A, is the nozzle we used in the earlier studies (cf. Heath et al.[24] and Khan et al.[23]). The two new nozzles have either a slower (nozzle B) or faster (nozzle C) expansion rate than nozzle A. The nominal cross-sectional area of the throat

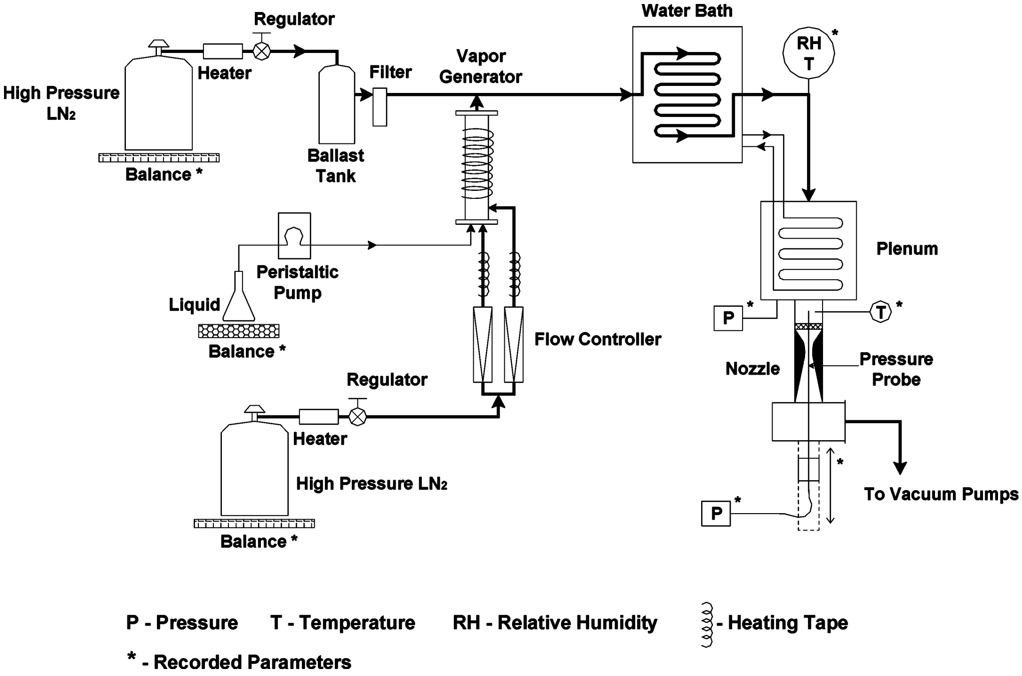

Figure 1. Schematic diagram of the setup used to conduct the current experiments.

A^* of the three nozzles is 63.5 mm^2. All of the nozzles have sidewalls containing 0.45-mm-thick silicon windows that are transparent to neutrons for the small-angle neutron scattering (SANS) experiments.

C. Pressure Measurements. Our nozzles are small enough that both the cross-sectional area of the throat A^* and the opening angle are sensitive to how the nozzle is assembled. Furthermore, as gas flows through the nozzle, boundary layers develop and change the effective dimensions of the nozzle from the original design. Thus, both A^* and the effective expansion rate depend on the stagnation pressure p_0. We use the pressure trace measurements to characterize each nozzle fully by determining A^*, the expansion rate, and the conditions under which condensation occurs as a function of the stagnation temperature and the condensable partial pressure.

We begin by measuring the pressure profile with only the carrier gas. We derive the value of A^* from the average mass flow rate through the nozzle at constant T_0 and p_0 using

$$A^* = \frac{\dot{m}_i/\mu_i}{p_0\left(\dfrac{\gamma+1}{2}\right)^{-\gamma/(\gamma-1)}}\left(\frac{RT_0}{\gamma\cdot\dfrac{\gamma+1}{2}}\right)^{1/2} \tag{3}$$

where $\dot{m}_i$ is the mass flow rate of N_2, μ_i is the molecular weight of nitrogen, R is the universal gas constant (8.314 J mol^{-1} K^{-1}), and $\gamma = C_p/C_v$ is the ratio of the heat capacity at constant pressure to the heat capacity at constant volume. For an isentropic expansion, the Mach number M, defined by the ratio of the local velocity v to the local speed of sound a, where $a = \sqrt{\gamma RT/\mu_i}$, is related to the measured pressure ratio by

$$M^2 = \frac{2}{\gamma-1}\left[\left(\frac{p}{p_o}\right)^{(1-\gamma)/\gamma} - 1\right] \tag{4}$$

The values of A/A^* are derived from the Mach number by solving

$$\frac{A}{A^*} = \frac{1}{M}\left[\frac{2+(\gamma-1)M^2}{\gamma+1}\right]^{(\gamma+1)/(2\gamma-2)} \tag{5}$$

We define the area expansion rate of the nozzle ($\mathrm{d}(A/A^*)/\mathrm{d}x$) as the slope of a straight-line fit to the $A(x)/A^*$ data. Alternatively, we can characterize the expansion rate for the nozzle in terms of the pressure[18,32] as $p^{-1}(\mathrm{d}p/\mathrm{d}t)$.

For dilute condensable gas mixtures, the mole fraction of condensable vapor in the gas stream y is determined from the mass flow measurements with adequate accuracy by

$$y = \frac{\dot{m}_v/\mu_v}{\dot{m}_i^0/\mu_i} \tag{6}$$

where $\dot{m}_i^0/\mu_i$ is the molar flow rate of the carrier gas through the nozzle at the same p_0 and T_0 and $\dot{m}_v/\mu_v$ is the molar flow rate of the condensable.

Using the measured area ratio, the stagnation conditions, the pressure trace measurements for the condensable mixture, and an equation of state as input, we integrate the diabatic flow equations to obtain the temperature, T, density, ρ, velocity, v, and the condensate mass fraction, g, at every point, x, in the nozzle.[31] From the temperature estimates, we define the onset of condensation as that point in the flow where the condensing flow temperature, T_{cf}, is 0.5 K higher than the temperature of an isentropic expansion of the same mixture T_{mi}.

We then determine the pressure of the condensable $p_v(x)$ as a function of position in the nozzle from

$$p_v(x) = yp_0\left(\frac{p(x)}{p_0}\right)\left(1 - \frac{g(x)}{g_\infty}\right) \tag{7}$$

where $g_\infty = \dot{m}_v/\dot{m}_i^0$. Finally, the supersaturation profile $S(x)$ is given by

$$S(x) = \frac{p_v(x)}{p_\infty(T(x))} \tag{8}$$

where $p_\infty(T(x))$ is the equilibrium vapor pressure of the condensable species. The temperature and supersaturation profiles and $A(x)$ are the input to the nucleation rate analysis described in section II.F.

D. Aerosol SANS Measurements. The aerosol SANS measurements are conducted on the NG7 SANS instrument at the National Institute of Standards and Technology (NIST) Center for Neutron Research (NCNR) in Gaithersburg, Maryland. Our experimental setup for the SANS measurement is identical to the one we use for the pressure trace measurement with two exceptions. First, the static pressure probe is completely removed from the nozzle. Second, the plenum, nozzle, and some downstream plumbing are placed in the NG7 SANS sample box with the neutron beam perpendicular to the flow in the nozzle. The windows separating the sample box from the neutron presample flight path and the detector tube are removed, and the entire system is evacuated to less than 13 Pa.

We use a neutron wavelength of $\lambda = 8$ Å with a wavelength spread of $\Delta\lambda/\lambda = 22\%$. To cover a reasonable range of scattering vector q, we use sample-to-detector distances (SDD) of 2.00 and 3.75 m. The scattered neutrons are detected by a 128 × 128 array of 0.25-cm^2 ^{3}He elements. A 12-mm-wide by 4-mm-high gadolinium aperture, centered 5.6 cm downstream from the throat, and the 12.5-mm nozzle thickness define the 600-mm^3 viewing volume. We intersperse 15−30-min measurements from the aerosol sample with about the same amount of background measurement to ensure that we always have a local background in case the windows become contaminated.

To extract the 1D SANS scattering spectra from the 2D scattering patterns, we use the NIST SANS data reduction package.[33] To summarize the data reduction protocol, we first subtract the background scattering from that of the sample. We then normalize the individual pixels by their sensitivity and convert the data to an absolute intensity scale, ignoring bad pixels and those at the edge of the detector. To create the $I(q)$ versus q spectrum, we must account for the Doppler shift in the momentum of the scattered neutrons that arises because the droplets are moving almost as fast as the 500-m s^{-1} neutrons.[34,35] The particle velocity required to make this correction comes from the pressure trace measurement. We then combine the spectra for the two SDDs without any further adjustments.

E. Fitting the SANS Data. To fit the scattering spectra, we first choose a distribution function. In our initial aerosol SANS work, we fit each spectrum to a Gaussian distribution of droplets.[36] More recently, we used a log−normal distribution of droplets.[22−24] In either case, the distributions are functions of the volume fraction of the droplets, ϕ, the geometric mean radius, the distribution width, and the contrast factor, $(\Delta\rho)^2$. Here, $\Delta\rho$ equals the scattering-length density of D$_2$O because the density of the N$_2$ carrier gas is almost 3 orders of magnitude lower and can be ignored.

The scattering intensity $I(q)$ for a log−normal distribution of droplets is

$$I_{\text{log-normal}}(q) = \frac{3\phi}{4\pi\langle r^3\rangle_{\text{log-normal}}}\frac{1}{\ln\sigma_{\text{r}}\sqrt{2\pi}}\int\frac{1}{r}\exp\left[-\frac{(\ln r - \ln r_{\text{g}})^2}{2\ln^2\sigma_{\text{r}}}\right]P(q,r)\,\text{d}r \quad (9)$$

where $P(q, r)$ is the particle form factor for spheres

$$P(q,r) = \left[\frac{4\pi(\sin(qr) - qr\cos(qr))}{q^3}\right]^2\Delta\rho^2 \quad (10)$$

and where r is the droplet radius, r_{g} is the median (geometric mean) radius of the size distribution, and $\ln(\sigma_{\text{r}})$ is the geometric standard deviation. The third moment of r for a log−normal distribution is

$$\langle r^3\rangle_{\text{log-normal}} = r_{\text{g}}^{\ 3}\exp\left[\frac{9}{2}\ln^2\sigma_{\text{r}}\right] \quad (11)$$

For a Gaussian distribution of droplets, the scattering intensity is

$$I_{\text{Gaussian}}(q) = \frac{3\phi}{4\pi\langle r^3\rangle_{\text{Gaussian}}}\frac{1}{\sigma_{\text{r}}\sqrt{2\pi}}\int\exp\left[-\frac{(\langle r\rangle - r)^2}{2\sigma_{\text{r}}^{\ 2}}\right]P(q,r)\,\text{d}r \quad (12)$$

where $\langle r\rangle$ is the number mean radius, σ_{r} is the width of the size distribution, and the third moment of r is

$$\langle r^3\rangle_{\text{Gaussian}} = \langle r\rangle^3\left[1 + 3\left(\frac{\sigma_{\text{r}}}{\langle r\rangle}\right)^2\right] \quad (13)$$

In either model, the aerosol number density is

$$N = \frac{3\phi}{4\pi\langle r^3\rangle} \quad (14)$$

We use the NIST data analysis procedures[37] to extract the best-fit parameters for ϕ, r_{g} or $\langle r\rangle$, ln σ_{r} or σ_{r}, and $\Delta\rho$. These procedures account for both the instrument resolution and the experimental uncertainty of the data. Because ϕ and $\Delta\rho$ are perfectly correlated, one of these is fixed and the other varies—we either assume a value for $\Delta\rho$ and optimize ϕ or we use the value of ϕ derived from the pressure trace measurements and optimize $\Delta\rho$.

F. Peak Nucleation Rate Analysis. To extract peak nucleation rates from the nozzle data, we apply the analysis method developed for laminar flow tubular reactor (LFTR) experiments.[6,7,38] We assume that the ratio of the maximum (peak) nucleation rate $J_{\text{exp}}^{\text{max}}$ to the particle production rate $\int J_{\text{exp}}\,\text{d}V$ is the same as that predicted by any reasonable nucleation theory,

$$\frac{J_{\text{exp}}^{\text{max}}}{\int J_{\text{exp}}\,\text{d}V} = \frac{J_{\text{theory}}^{\text{max}}}{\int J_{\text{theory}}\,\text{d}V} = \frac{1}{V_{J_{\max}}} \quad (15)$$

where $V_{J_{\max}}$ is the characteristic volume corresponding to the maximum nucleation rate. The characteristic time corresponding to $J_{\max}$ is

$$\Delta t_{J_{\max}} = \frac{V_{J_{\max}}}{\dot{V}_{\text{NZ}}} \quad (16)$$

where $\dot{V}_{\text{NZ}}$ is the volumetric flow rate in the nucleation zone, $\dot{V}_{\text{NZ}} = (\dot{m}_{\text{i}} + \dot{m}_{\text{v}})/\rho_{\text{NZ}} \approx \dot{m}_{\text{i}}^0/\rho_{\text{NZ}}$, and ρ_{NZ} is the density of the gas in the nucleation zone. Finally, the peak nucleation rate is

$$J_{\max}(S_{J_{\max}}, T_{J_{\max}}) = \frac{N}{\Delta t_{J_{\max}}}f_{\text{exp}} \quad (17)$$

where $f_{\text{exp}} = \rho_{\text{NZ}}/\rho_{\text{VV}}$ corrects for the continued expansion of the gas between the nucleation zone and the viewing volume. In eq 17, N comes from SANS experiments and assumes that the particles formed in the nucleation zone do not coagulate, and all other quantities are calculated using data obtained from the pressure trace experiments.

TABLE 1: Area of the Throat A^*[a]

	A^* (mm^2) (from calibration)	d(A/A^*)/dx (cm^{-1})	p^{-1} dp/dt (s^{-1})
nozzle A	59.1	0.0486	4700
nozzle B	59.3	0.0385	4100
nozzle C	58.2	0.0786	6500

[a] For all three nozzles, A^* was designed to be 63.5 mm^2. The flow-rate measurements used to determine A^* experimentally were made at $p_0 = 59.7$ kPa and $T_0 = 298$ K. For d(A/A^*)/dx, the slope is constant between 1 and 7 cm downstream from the throat. The local expansion rate p^{-1} dp/dt decreases by approximately 50% between 1 and 7 cm downstream from the throat. The rates given here correspond to the averages.

The classical nucleation theory (CNT) by Becker and Döring[39] gives the nucleation rate, J_{BD}, as

$$J_{BD} = \sqrt{\frac{2\sigma}{\pi\mu_v}}\,v_m\left(\frac{p_v}{kT}\right)^2 \exp\left\{\frac{-16\pi v_m^{\,2}\sigma^3}{3(kT)^3(\ln S)^2}\right\} \tag{18}$$

where σ is the surface tension of the macroscopic fluid−vapor interface, v_m is the molecular volume, and k is the Boltzmann constant. The empirical correction function developed by Wölk and Strey[13] to predict measured water nucleation rates is

$$J_{H_2O} = J_{BD}\exp\left(-27.56 + \frac{6.5 \times 10^3}{T}\right) \tag{19}$$

for H_2O and

$$J_{D_2O} = J_{BD}\exp\left(-35.98 + \frac{8.6 \times 10^3}{T}\right) \tag{20}$$

for D_2O.

IV. Results and Discussion

A. Pressure Trace Experiments. We held the stagnation pressure p_0 for our experiments at 59.7 ± 0.01 kPa, and T_0 was 15, 25, or 35 °C. We started by making a limited set of H_2O experiments to confirm that the onset measurements for nozzle A were consistent with our previous results[23,30] and to confirm that the expansion rates of nozzles B and C were reasonable and significantly different from that of nozzle A. Table 1 summarizes the values of A^* and the expansion rates for the three nozzles measured at $T_0 = 298$ K. For comparison, in the nucleation pulse chambers $p^{-1}(\mathrm{d}p/\mathrm{d}t)$ is approximately 100. Table 2 summarizes the results of the current H_2O measurements. In the experimental temperature range, 205−235 K, the agreement between the current and earlier data sets is within experimental error.

We then turned to the D_2O condensation experiments. To reach our target temperatures of 210, 220, and 230 K, we used stagnation temperatures of $T_0 = 25$ and 35 °C for nozzles A and C. For nozzle B, we also ran a series of experiments with $T_0 = 15$ °C. Because nozzle B has a slower expansion rate but the same physical length as the other nozzles, the range of onset temperatures that can be reached from a given stagnation temperature is more restricted than in the faster nozzles (A, C). Table 3 summarizes the stagnation conditions and onset conditions for the D_2O pressure trace experiments. Again, the agreement between the current data set and our earlier work[23,30] is very good over the appropriate temperature range.

Figure 2a is a Wilson plot of the current D_2O data set for the three nozzles. Despite the difference in expansion rates, we find that the onset data for the three nozzles are rather similar, especially around 230 K. The onset data only begin to differ at lower temperatures (~210 K). At constant onset temperature, the onset pressures increase in the order of increasing expansion rate (i.e., nozzle B, nozzle A, and nozzle C). As expected, faster expansions probe the metastable region more deeply.

TABLE 2: Results of Pressure Trace Experiments for H_2O[a]

nozzle	$\dot{m}_{H_2O}$/ g min^{-1}	p_0/kPa	T_0/K	p_{on}/kPa	T_{on}/K	$p_{J_{max}}$/kPa	$T_{J_{max}}$/K
A	1.99	59.7	309.38	0.086	203.76	0.086	203.64
A	2.66	59.7	309.39	0.124	208.61	0.123	207.98
A	3.99	59.7	309.38	0.209	215.25	0.208	215.08
A	5.29	59.6	309.38	0.300	220.42	0.298	220.10
A	6.63	59.7	309.39	0.401	224.41	0.397	224.04
A	7.96	59.7	309.40	0.505	227.65	0.501	227.30
A	9.27	59.7	309.39	0.616	230.64	0.610	230.29
B	1.34	59.7	288.13	0.075	203.76	0.075	203.25
B	2.00	59.7	288.13	0.126	210.38	0.125	210.16
B	2.67	59.7	288.13	0.183	215.54	0.181	215.13
B	3.34	59.7	288.14	0.246	220.15	0.244	219.80
B	4.02	59.7	288.15	0.312	223.43	0.311	223.31
B	2.02	59.7	298.14	0.112	207.77	0.112	207.64
B	2.68	59.7	298.13	0.162	213.02	0.161	212.67
B	3.35	59.7	298.15	0.216	216.80	0.216	216.73
B	4.02	59.7	298.16	0.273	219.99	0.271	219.69
B	2.00	59.6	309.38	0.094	205.85	0.093	205.41
B	2.63	59.7	309.40	0.131	209.76	0.131	209.80
B	3.97	59.7	309.38	0.222	216.64	0.220	216.37
B	5.26	59.6	309.41	0.318	221.60	0.314	221.23
B	6.62	59.6	309.41	0.428	225.94	0.424	225.54
B	8.00	59.6	309.40	0.544	229.29	0.540	229.00
B	9.25	59.7	309.40	0.657	232.20	0.654	231.96
C	2.67	59.6	309.39	0.115	205.10	0.114	204.73
C	3.35	59.6	309.39	0.154	209.22	0.154	209.20
C	4.64	59.7	309.40	0.249	216.16	0.246	215.65
C	5.32	59.7	309.40	0.284	218.28	0.280	217.72
C	6.66	59.6	309.41	0.375	221.61	0.375	221.64
C	7.98	59.6	309.40	0.477	225.48	0.471	224.88
C	9.99	59.7	309.39	0.646	230.63	0.631	229.42

[a] Here, $\dot{m}_{H_2O}$ is the mass flow rate of H_2O, p_0 and T_0 are the stagnation pressure and temperature, p_{on} and T_{on} are the onset pressure and temperature, and $p_{J_{max}}$ and $T_{J_{max}}$ are the pressure and temperature corresponding to the maximum nucleation rate.

Although onset is a widely used term, its definition varies among different research groups. We define onset as that point in the flow where the temperature of the condensing flow deviates by 0.5 K from the temperature of an isentropic expansion of the same gas mixture through the same nozzle.[31] Because droplet growth is primarily responsible for heat release to the flow, onset is affected both by the rate of droplet production and the rate of droplet growth. For nucleation rate measurements, however, we are more interested in the pressure $p_{J_{max}}$ and temperature $T_{J_{max}}$ that correspond to the maximum nucleation rate. We include these values for both H_2O and D_2O in Tables 2 and 3. Figure 2b is a modified Wilson plot that shows $p_{J_{max}}$ as a function of $T_{J_{max}}$. The trends in Figure 2b are the same as those in Figure 2a, but now the correlation lines for the three nozzles are separated over the entire temperature range and the lines are essentially parallel. The most important aspect of Figure 2b is that by using different nozzles we can reach different values of $p_{J_{max}}$ at a fixed value of $T_{J_{max}}$ or, equivalently, three different supersaturations at the same $T_{J_{max}}$. Thus, the peak nucleation rates in these nozzles should be significantly different, and we will be able to determine how the nucleation rates at constant temperature vary as a function of supersaturation. Although Figure 2b demonstrates the feasibility of our approach, it does not directly yield the operating conditions for each nozzle.

TABLE 3: Results of Pressure Trace Experiments for D_2O^a

nozzle	$\dot{m}_{D_2O}$/ g min^{-1}	p_0/kPa	T_0/K	p_{on}/kPa	T_{on}/K	$p_{J\max}$/kPa	$T_{J\max}$/K
A	1.75	59.7	298.15	0.084	207.56	0.082	206.84
A	2.03	59.7	298.13	0.104	209.86	0.102	209.31
A	2.18	59.6	298.14	0.110	210.90	0.110	210.91
A	2.31	59.7	298.14	0.120	212.20	0.119	211.83
A	2.47	59.7	298.15	0.130	213.44	0.128	212.81
A	2.62	59.7	298.14	0.140	214.28	0.139	213.96
A	3.49	59.7	298.16	0.202	219.22	0.201	218.86
A	4.35	59.7	298.15	0.274	222.79	0.272	222.46
A	5.80	59.7	298.15	0.398	228.24	0.394	227.88
A	2.33	59.7	308.13	0.107	209.76	0.106	209.05
A	3.49	59.7	308.16	0.174	216.60	0.173	216.32
A	4.37	59.6	308.17	0.235	219.50	0.234	219.32
A	4.49	59.7	308.14	0.240	220.76	0.238	220.54
A	4.50	59.7	308.15	0.240	220.79	0.238	220.48
A	4.65	59.7	308.12	0.251	221.44	0.247	220.89
A	5.80	59.7	308.18	0.331	225.10	0.329	224.88
A	6.98	59.7	308.16	0.432	228.34	0.430	228.09
A	7.71	59.7	308.16	0.488	229.86	0.482	229.52
A	7.85	59.7	308.13	0.503	230.56	0.498	230.16
A	7.98	59.7	308.14	0.499	230.97	0.492	230.54
A	8.05	59.7	308.15	0.502	230.85	0.496	230.46
A	8.23	59.7	308.17	0.518	231.57	0.514	231.11
B	1.12	59.7	288.13	0.060	204.94	0.058	203.94
B	1.41	59.6	288.14	0.079	208.03	0.078	207.74
B	1.54	59.7	288.15	0.089	209.68	0.088	209.16
B	1.71	59.7	288.12	0.100	211.64	0.099	211.38
B	1.67	59.7	288.13	0.099	211.02	0.098	210.77
B	2.25	59.7	288.14	0.144	216.18	0.143	215.91
B	2.84	59.7	288.14	0.191	220.30	0.189	219.83
B	3.36	59.7	288.17	0.242	223.41	0.242	223.31
B	2.26	59.7	298.14	0.125	213.10	0.124	212.87
B	3.10	59.7	298.15	0.188	218.81	0.186	218.36
B	3.22	59.7	298.15	0.196	219.18	0.195	218.88
B	3.42	59.7	298.14	0.209	221.01	0.208	220.83
B	3.36	59.7	298.16	0.197	220.19	0.195	219.81
B	3.96	59.7	298.15	0.256	222.91	0.254	222.63
B	4.57	59.7	298.16	0.307	225.33	0.304	225.05
B	2.83	59.7	308.15	0.146	215.14	0.143	214.28
B	4.10	59.7	308.14	0.232	220.93	0.232	220.95
B	5.66	59.7	308.15	0.350	226.74	0.348	226.45
B	6.78	59.7	308.15	0.438	229.76	0.436	229.54
B	7.04	59.7	308.15	0.458	230.18	0.457	230.06
B	7.18	59.7	308.16	0.459	230.51	0.461	230.58
B	7.94	59.7	308.17	0.523	232.53	0.524	232.53
C	2.33	59.7	298.15	0.118	209.95	0.117	209.38
C	2.47	59.7	298.15	0.127	210.96	0.125	210.30
C	2.61	59.7	298.16	0.136	211.88	0.135	211.36
C	2.82	59.7	298.16	0.150	213.23	0.148	212.55
C	3.50	59.7	298.14	0.199	216.93	0.196	216.27
C	4.65	59.7	298.14	0.291	223.05	0.285	221.88
C	4.09	59.7	308.12	0.202	217.11	0.200	216.65
C	4.81	59.7	308.14	0.260	220.02	0.254	219.14
C	4.93	59.6	308.15	0.268	220.41	0.261	219.25
C	5.05	59.7	308.16	0.277	220.89	0.272	220.06
C	5.23	59.7	308.16	0.278	221.66	0.275	221.06
C	5.36	59.7	308.18	0.285	221.64	0.281	221.08
C	5.52	59.6	308.14	0.299	222.81	0.296	222.26
C	5.84	59.7	308.11	0.321	223.76	0.316	223.05
C	6.98	59.7	308.13	0.411	228.25	0.392	225.73
C	8.66	59.7	308.15	0.581	233.97	0.533	229.25
C	8.84	59.7	308.16	0.554	232.32	0.532	230.15

[a] Here, $\dot{m}_{D_2O}$ is the mass flow rate of D_2O, p_0 and T_0 are the stagnation pressure and temperature, p_{on} and T_{on} are the onset pressure and temperature, and $p_{J\max}$ and $T_{J\max}$ are the pressure and temperature corresponding to the maximum nucleation rate.

To determine the operating conditions, we correlate both $p_{J_{\max}}$ and $T_{J_{\max}}$ with the mass flow rate of D_2O, $\dot{m}_{D_2O}$. As shown in Figure 3, at fixed T_0 both $p_{J_{\max}}$ and $T_{J_{\max}}$ correlate very well with $\dot{m}_{D_2O}$. Figure 3 illustrates only the results for nozzle A, but the results for nozzles B and C are similar. These graphs enable us to select the values of T_0 and $\dot{m}_{D_2O}$ required to obtain the desired values of $T_{J_{\max}}$ and, consequently, to obtain a series of nucleation rates under isothermal conditions. Figure 3a also shows that the operating conditions that lead to $T_{J_{\max}}$ are not unique. In particular, $T_{J_{\max}}$ can be obtained from different combinations of the stagnation temperature and the condensable flow rate. For example, in nozzle A $T_{J_{\max}} = 210$ K can be reached using either $T_0 = 25$ °C and $\dot{m}_{D_2O} = 2.04$ g/min or $T_0 = 35$ °C and $\dot{m}_{D_2O} = 2.33$ g/min. The physical location in the nozzle that corresponds to $T_{J_{\max}} = 210$ K is, of course, quite different. Figure 4 illustrates the condensation process for these two cases in terms of the fraction of incoming material that has condensed. When $T_0 = 25$ °C, condensation begins at a position $x = 3.4$ cm downstream of the throat, and $T_{J_{\max}}$ occurs at $x = 3.52$ cm. When $T_0 = 35$ °C, condensation starts at $x = 4.5$ cm, and $T_{J_{\max}}$ occurs at $x = 4.99$ cm. Because we measure the neutron scattering spectra between 5.0 and 6.2 cm downstream of the throat (indicated by the gray region in Figure 4), we would like to ensure that droplet growth is essentially complete by the time the aerosol reaches the viewing volume (i.e., the condensation curve has leveled off). Thus, to measure the nucleation rate at $T = 210$ K in nozzle A, starting the expansion at $T_0 = 25$ °C and $\dot{m}_{D_2O} = 2.04$ g/min improves our ability to measure N accurately.

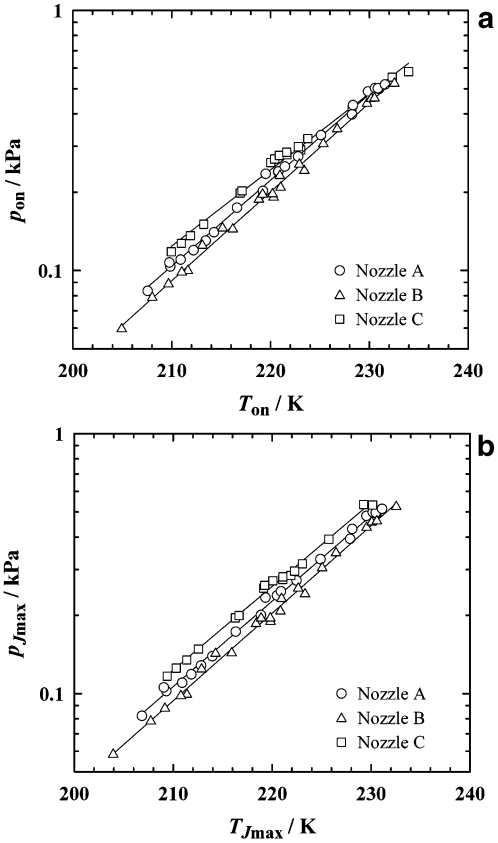

Figure 2. (a) Onset pressure plotted as a function of the onset temperature for the D_2O pressure trace experiments with nozzles A, B, and C. (b) Same experimental results presented in terms of the pressure and temperature corresponding to the maximum nucleation rates. Note that now the curves corresponding to each nozzle are cleanly separated, and it is clear that we can achieve three distinct supersaturations at a fixed temperature.

B. Aerosol SANS Experiments. Our primary objective was to measure the peak nucleation rates at $T_{J_{\max}} = 210$, 220, and 230 K in each nozzle. Table 4 summarizes the operating conditions as well as $p_{J_{\max}}$ and $T_{J_{\max}}$ for the actual SANS

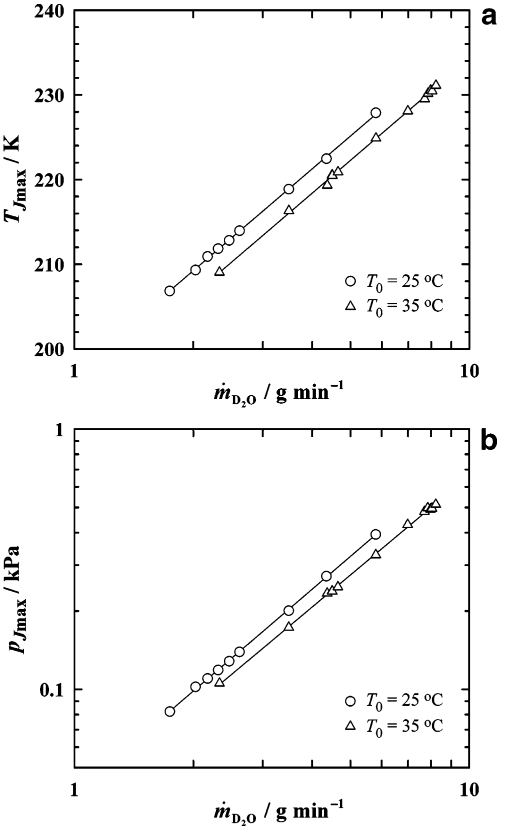

Figure 3. Both (a) $T_{J_{\max}}$ and (b) $p_{J_{\max}}$ correlate well with the mass flow rate of D_2O entering the nozzle, $\dot{m}_{D_2O}$.

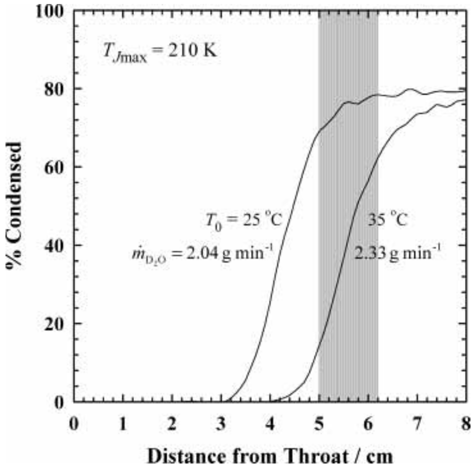

Figure 4. Degree of condensation, as characterized by the percentage of the initial vapor that has condensed, shown as a function of position in the nozzle for two different initial operating conditions that both result in $T_{J_{\max}}$ = 210 K. The shaded region corresponds to the SANS viewing volume. For the SANS experiment, working at the lower stagnation temperature is preferred because condensation is almost complete in the region where the aerosol is characterized.

TABLE 4: Operating Conditions for the SANS Experiment

nozzle	$T_{J_{\max}}$[a]/K	p_0/kPa	T_0/K	$\dot{m}_{D_2O}$/g min^{-1}	$T_{J_{\max}}$[b]/K	$p_{J_{\max}}$/kPa
A	210	59.6	298.15	2.04	209.57	0.1007
A	220	59.6	308.15	4.63	220.93	0.2493
A	230	59.6	308.15	7.68	229.72	0.4749
B	210	59.6	288.15	1.61	210.15	0.0927
B	220	59.6	298.15	3.36	219.84	0.2034
B	230	59.6	308.15	7.00	230.15	0.4501
C	210	59.6	298.15	2.48	210.36	0.1258
C	220	59.6	308.15	4.96	219.88	0.2590
C	230	59.6	308.15	8.86	229.97	0.5391
A − H_2O	230	59.6	308.15	9.16	229.76	0.6007

[a] Desired. [b] Actual; derived from correlations of $\dot{m}_{D_2O}$ vs $T_{J_{\max}}$ (Figure 3a).

experiments. The values are based on correlations such as those illustrated in Figure 3a and b. The averaged 1D scattering spectra measured for all of the experiments are shown in Figure 5.

We analyzed all of the spectra using the same procedure. We assumed that the aerosol size distributions were either Gaussian or log−normal and determined the best-fit parameters following the procedures detailed in section II.E. When $\Delta\rho$ was fixed, we assumed that it was equal to 6.36×10^{10} cm^{-2}, the scattering-length density of D_2O at 0 °C.[24] In the viewing volume, the temperature varies between 195 and 242 K, and we assume that the temperature of the droplets is the same as that of the surrounding gas. Although the bulk density of D_2O decreases with decreasing temperature, thereby reducing the scattering-length density, the high internal pressure of the small droplets almost completely compensates for this effect. Nevertheless, we also reduced the scattering data by fixing the volume fraction of droplets ϕ to equal that derived from the pressure trace measurements and varied $\Delta\rho$ instead.

Table 5 summarizes all of the fit parameters using the four possible combinations of the two underlying assumptions. Because the nucleation rate depends directly on the value of N found by fitting the spectra, it is important to assess, at least once, how much N varies as a function of the particular set of assumptions that underlie the fit. Overall, we see that the ratio of the minimum to the maximum value of N is always between 0.67 and 0.91 and that the value of N calculated for the log−normal size distribution is always less than or equal to that for the equivalent Gaussian fit.

Because N is derived from ϕ, we would like to determine if there are physical reasons that ϕ_{SANS}/ϕ_{PT}, or alternatively $\Delta\rho_{SANS}/\Delta\rho_{D_2O}$, is not always equal to unity. Thus, using the fits for the log−normal size distribution, we plotted ϕ_{SANS}/ϕ_{PT} as a function of a number of different variables including the position at the maximum nucleation rate, the mass flow rate of D_2O, the average particle size, and so forth. The most consistent correlation was obtained with the position at the maximum nucleation rate, $x_{J_{\max}}$, in the nozzle, and this is illustrated in Figure 6. We note that there is good agreement between the current data (filled symbols) and those of Khan et al.[23] (circles with cross hairs) that were measured 1 year earlier. Even the data from Heath et al.[24] (open diamonds), measured using an older neutron detector, agree reasonably well with the current values. When the maximum nucleation rate occurs far enough upstream, the data are somewhat scattered but are generally clustered around 1. As $x_{J_{\max}}$ approaches the viewing volume ($x_{J_{\max}} > \sim$2.8 cm), the disagreement gets worse (i.e., ϕ_{SANS} is distinctly lower than ϕ_{PT}).

We have identified two possible reasons for this discrepancy. One reason may be that, as illustrated in Figure 4, the aerosol formed close to the viewing volume is still growing rapidly. Intuitively, the scattering signal from an aerosol sample that is evolving across the viewing volume should yield a spectrum that is consistent with a more polydisperse aerosol than the true sample at any fixed location. We plan to address the question of how this broadening affects the value of ϕ_{SANS} calculated from the fit parameters by simulation and postpone a discussion of this issue to a later date. A second issue relates to small changes in the expansion when the nozzle operates with the surroundings at low pressure ($\sim$10 Pa), as in the sample box at NIST, rather than at atmospheric pressure. We conducted a limited number of experiments and found that for nozzle C the

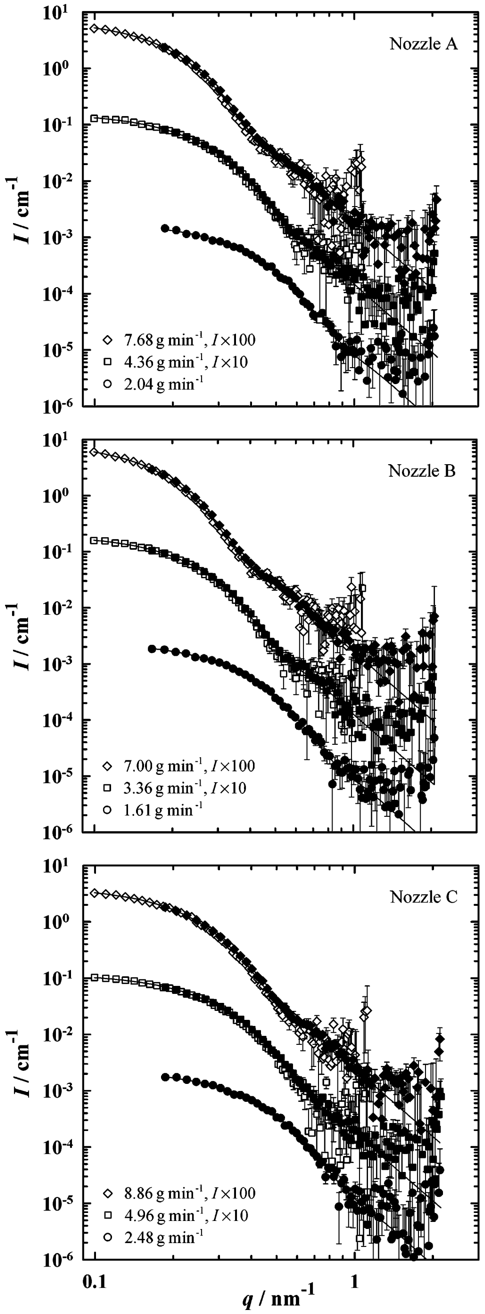

Figure 5. One-dimensional SANS spectra. In each plot, the lowest curve is at the true absolute intensity, and the other curves are offset by factors of 10 and 100, respectively. Open symbols correspond to the measurements at a sample-to-detector distance (SDD) of 3.75 m, and solid symbols correspond to an SDD of 2.00 m. Solid lines are fits to the data assuming log−normal aerosol size distributions with $\Delta\rho = 6.36 \times 10^{10}$ cm^{-2}.

pressure external to the nozzle had no effect on the expansions. In nozzles A and B, the expansion rates were slightly reduced when the external pressure was decreased to 130 Pa, and onset occurred a little further downstream. The changes were small enough that the data still agree with the Wilson plots shown in Figure 2, but ϕ_{PT} in the viewing volume can be up to 15% lower than the corresponding measurement in an atmospheric pressure environment.

We also checked whether $\Delta\rho_{SANS}/\Delta\rho_{D_2O}$ varies systematically with the density inside the droplet. To do this, we assumed that the droplets are at the same temperature as the gas in the viewing volume and calculated the pressure inside the droplets using the Laplace equation and the average droplet radius. Because changes in density due to the decreased temperature generally cancel those due to the increases in pressure, we found that the most ρ_{D_2O} varied was about 5%. This is equivalent to changing ϕ by about 10% and is not enough to explain the observations in Figure 6. Furthermore, the predicted change in the scattering-length density is often in the opposite direction to that predicted by letting $\Delta\rho_{D_2O}$ float.

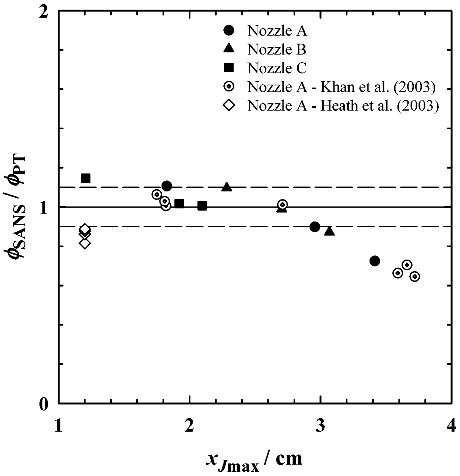

Figure 6. ϕ_{SANS}/ϕ_{PT}, calculated using the log−normal fit parameters, decreases systematically with the location of the onset of condensation. This suggest that in order to get good agreement between these two values it is important to ensure that the aerosol has evolved fully before making the SANS measurement.

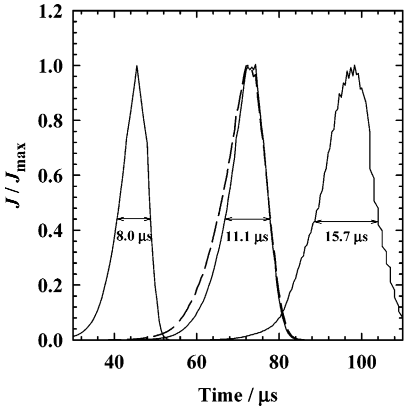

Figure 7. Three normalized nucleation pulses calculated for D_2O condensation in nozzle A. Solid lines were calculated using eq 20, and the dashed line corresponds to CNT (eq 18). The origin of the time axis corresponds to the throat. As the onset of condensation moves downstream, the nucleation pulse increases by about a factor of 2 in this nozzle.

In conclusion, although we do not always have perfect mass balance, the agreement between the two experiments is improved when the onset is at least 2 cm upstream from the edge of the SANS viewing volume. For now, we will calculate the nucleation rate using the value of N derived from the log−normal fits and with $\Delta\rho_{D_2O}$ fixed. All of the other options are within the error bars of the experiments.

C. Nucleation Pulse. To determine the length of the nucleation pulse, we use the supersaturation and temperature profiles derived from the pressure trace measurements to evaluate the nucleation rates in eq 15. Figure 7 illustrates the nucleation rates, normalized by the peak rate, as a function of time for three different experiments in nozzle A. The solid lines correspond to the calculation using the temperature-corrected version of CNT (eq 20). The dashed line corresponds to standard CNT (eq 18) and is included for only one of the cases. The

TABLE 5: Best-Fit Parameters Derived from the SANS Spectra[a]

nozzle D_2O flow rate	distribution	$\Delta\rho$/cm^{-2}	ϕ	r_g or $\langle r \rangle$ /nm	ln σ_r or $\sigma/\langle r \rangle$	$N/10^{11}$ cm^{-3}
nozzle A 2.04 g min^{-1}	log−normal	*6.36×10^{10}*	5.50×10^{-7}	4.6	0.235	10.6
	log−normal	5.42×10^{10}	*7.59×10^{-7}*	4.6	0.235	14.6
	Gaussian	*6.36×10^{10}*	5.62×10^{-7}	4.2	0.365	13.1
	Gaussian	5.47×10^{10}	*7.59×10^{-7}*	4.2	0.365	17.7
nozzle A 4.36 g min^{-1}	log−normal	*6.36×10^{10}*	1.38×10^{-6}	7.1	0.219	7.3
	log−normal	6.03×10^{10}	*1.54×10^{-6}*	7.1	0.219	8.1
	Gaussian	*6.36×10^{10}*	1.41×10^{-6}	6.8	0.303	8.4
	Gaussian	6.08×10^{10}	*1.54×10^{-6}*	6.8	0.303	9.2
nozzle A 7.68 g min^{-1}	log−normal	*6.36×10^{10}*	2.58×10^{-6}	10.2	0.184	4.9
	log−normal	6.69×10^{10}	*2.33×10^{-6}*	10.2	0.184	4.4
	Gaussian	*6.36×10^{10}*	2.59×10^{-6}	10.2	0.214	5.3
	Gaussian	6.71×10^{10}	*2.33×10^{-6}*	10.2	0.214	4.6
nozzle B 1.61 g min^{-1}	log−normal	*6.36×10^{10}*	6.24×10^{-7}	4.9	0.229	10.6
	log−normal	5.94×10^{10}	*7.16×10^{-7}*	4.9	0.229	11.4
	Gaussian	*6.36×10^{10}*	6.40×10^{-7}	4.4	0.358	12.6
	Gaussian	6.01×10^{10}	*7.16×10^{-7}*	4.4	0.358	14.1
nozzle B 3.36 g min^{-1}	log−normal	*6.36×10^{10}*	1.34×10^{-6}	8.0	0.202	5.2
	log−normal	6.33×10^{10}	*1.36×10^{-6}*	8.0	0.202	5.3
	Gaussian	*6.36×10^{10}*	1.36×10^{-6}	7.8	0.258	5.7
	Gaussian	6.36×10^{10}	*1.36×10^{-6}*	7.8	0.258	5.7
nozzle B 7.00 g min^{-1}	log−normal	*6.36×10^{10}*	2.43×10^{-6}	11.1	0.187	3.6
	log−normal	6.66×10^{10}	*2.22×10^{-6}*	11.1	0.187	3.3
	Gaussian	*6.36×10^{10}*	2.44×10^{-6}	11.1	0.217	3.8
	Gaussian	6.68×10^{10}	*2.22×10^{-6}*	11.1	0.217	3.4
nozzle C 2.48 g min^{-1}	log−normal	*6.36×10^{10}*	7.81×10^{-7}	4.4	0.238	17.1
	log−normal	6.38×10^{10}	*7.76×10^{-7}*	4.4	0.238	17.0
	Gaussian	*6.36×10^{10}*	8.00×10^{-7}	3.9	0.379	21.7
	Gaussian	6.46×10^{10}	*7.76×10^{-7}*	3.9	0.379	21.0
nozzle C 4.96 g min^{-1}	log−normal	*6.36×10^{10}*	1.50×10^{-6}	6.1	0.233	12.2
	log−normal	6.42×10^{10}	*1.47×10^{-6}*	6.1	0.233	12.0
	Gaussian	*6.36×10^{10}*	1.52×10^{-6}	5.7	0.345	14.6
	Gaussian	6.48×10^{10}	*1.47×10^{-6}*	5.7	0.345	14.1
nozzle C 8.86 g min^{-1}	log−normal	*6.36×10^{10}*	2.64×10^{-6}	8.0	0.214	10.1
	log−normal	6.81×10^{10}	*2.31×10^{-6}*	8.0	0.214	8.8
	Gaussian	*6.36×10^{10}*	2.67×10^{-6}	7.8	0.272	11.1
	Gaussian	6.84×10^{10}	*2.31×10^{-6}*	7.8	0.272	9.6
nozzle A H_2O 9.16 g min^{-1}	log−normal	*-5.59×10^{9}*	3.51×10^{-6}	12.1	0.121	4.4
	log−normal	-6.37×10^{9}	*2.70×10^{-6}*	12.1	0.114	3.4
	Gauss	*-5.59×10^{9}*	3.62×10^{-6}	11.6	0.193	5.0
	Gauss	-6.38×10^{9}	*2.70×10^{-6}*	12.1	0.127	3.4

[a] Italicized values were fixed during the fitting process.

origin for the time axis, $t = 0$, corresponds to the throat. Figure 7 demonstrates that, close to the throat, the nucleation pulse is sharp and there is little ambiguity in the choice of $S_{J_{\max}}$ and $T_{J_{\max}}$. Further downstream, the profiles are broader, and there are often short regions where J is essentially constant (i.e., changes in supersaturation compensate for changes in temperature). In these cases, any of the ($S_{J_{\max}}$, $T_{J_{\max}}$) pairs are appropriate. Finally, comparing the curve calculated using CNT with that calculated including the temperature correction, we see that incorporating the temperature correction decreases $\Delta t_{J_{\max}}$ systematically by up to 20%. This is because the temperature correction decreases the temperature dependence of CNT, and thus changes in T cannot compensate for rapid changes in S as easily and the nucleation pulse is sharpened. All nucleation rates reported below were calculated using our estimates for $\Delta t_{J_{\max}}$ based on eq 20.

Temperature and supersaturation change very rapidly in the nozzle. To ensure that our assumption of steady-state nucleation is appropriate, we estimated the time required to reach the steady-state nucleation rate in response to a step change in supersaturation. We used an equation developed by Wilemski[40] that is known[41] to overestimate the actual time by about 40%. Even under the most extreme conditions, the estimated time lags are always less than 1 μs. In contrast, the time required to change the supersaturation from 1 to $S_{\max}$ is always greater than 10 μs, which is ample time for the evolving cluster size distribution to adjust to the changing conditions. The results[42] of detailed kinetic modeling of cluster formation in nozzles with and without the steady-state assumption also support the validity of assuming a stationary nucleation process.

D. Water Nucleation Rates and Comparisons with Previous Results. Figure 8 summarizes the D_2O nucleation rates measured in this study and notes the exact values of $T_{J_{\max}}$. Before discussing the accuracy of these measurements, we compare them with the predictions of classical nucleation theory (CNT), shown as the dashed lines. At the highest temperature, the predictions of CNT lie slightly below the experimental points but are still within experimental error. At the lower temperatures, the classical predictions lie well below the measured values. The discrepancy increases as the temperature is lowered and exceeds the measurement error bars. In contrast, the predictions of the empirical temperature correction function to the classical

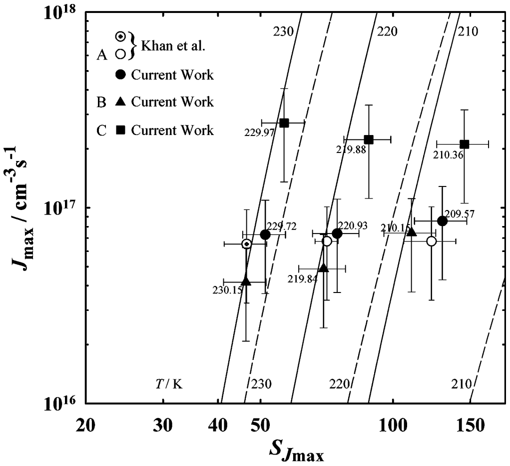

Figure 8. Maximum nucleation rates measured in the nozzles as a function of supersaturation and temperature. Values of $T_{J_{max}}$ are noted beside each point. For the data from Khan et al.,[23] the open circle marked with a crosshair is his measurement at 230 K. The other open circles are interpolated points based on his correlations of $S_{J_{max}}$ and $T_{J_{max}}$ with $\dot{m}_{D_2O}$. Solid lines are the predictions of the empirical function for the nucleation rate of D_2O from Wölk and Strey[13] (eq 20). Dashed lines are the predictions of classical nucleation theory (eq 18).

theory proposed by Wölk and Strey[13] (solid lines) lie within the error bars for nearly all of the experimental data points.

The overall uncertainty assigned to J_{max} is ±50% and is based on the uncertainties in N and $\Delta t_{J_{max}}$. We estimated the errors in $S_{J_{max}}$ assuming that $T_{J_{max}}$ has a potential systematic error of ±1K. We see that we were able to determine nucleation rates as a function of supersaturation at constant temperature. As expected, the highest nucleation rates are found in nozzle C, followed by those in nozzles A and B. The nucleation rates for nozzle A are again very close to constant, and there is excellent quantitative agreement at 230 K with the point measured by Khan et al.[23] We also used the correlations between $\dot{m}_{D_2O}$ and $T_{J_{max}}$ or $S_{J_{max}}$ developed by Khan et al.[23] to determine average values of $S_{J_{max}}$ corresponding to $T_{J_{max}} = 220$ and 210 K and assigned $J = 6.74 \times 10^{16}$ to these values. Again, these data show good agreement with the current nozzle A data set. Although the peak rates in nozzle C appear to decrease slightly while those in nozzle B increase slightly as $T_{J_{max}}$ decreases, even for these nozzles the rates are still constant with respect to the quoted error bars.

As noted in Figure 8 as well as in Table 4, the values of $T_{J_{max}}$ for the SANS experiments are not exactly 210, 220, and 230 K. Figure 8, however, suggests that it is acceptable to use the mass flow rate correlations to find the value of $S_{J_{max}}$ corresponding to the desired temperature. Because the temperature shifts are rather small and the nucleation rates are almost constant in our range, there is no need to adjust the nucleation rate itself. The values of $S_{J_{max}}$ in Table 6 and those plotted in Figure 9 have been adjusted to match the desired temperatures.

TABLE 6: Isothermal Nucleation Rates

nozzle	$\dot{m}_{D_2O}$/g min^{-1}	$S_{J_{max}}$ [a]	$S_{J_{max}}$ [b]	$\Delta t_{J_{max}}$/ 10^{-6} s	ρ_{NZ}/ ρ_{VV}	$N/10^{11}$ cm^{-3}	$J/10^{16}$ cm^{-3} s^{-1}
A	2.04	129.6	127.1	14.2	1.16	10.6	8.6
A	4.63	74.7	78.1	11.8	1.19	7.3	7.4
A	7.68	51.3	50.7	8.7	1.29	4.9	7.3
B	1.61	110.3	111.3	15.7	1.17	10.6	7.4
B	3.36	69.6	59.0	12.7	1.18	5.2	4.9
B	7.00	46.3	46.6	10.5	1.20	3.6	4.2
C	2.48	145.4	148.8	11.5	1.42	17.1	21.1
C	4.96	88.1	87.6	7.8	1.43	12.2	22.3
C	8.86	56.6	56.5	5.9	1.59	10.1	27.1
A − H_2O	9.16	44.3	45.0	8.7	1.28	4.4	6.6

[a] Calculated for the actual $T_{J_{max}}$ in Table 4. [b] Calculated for the desired $T_{J_{max}}$ in Table 4.

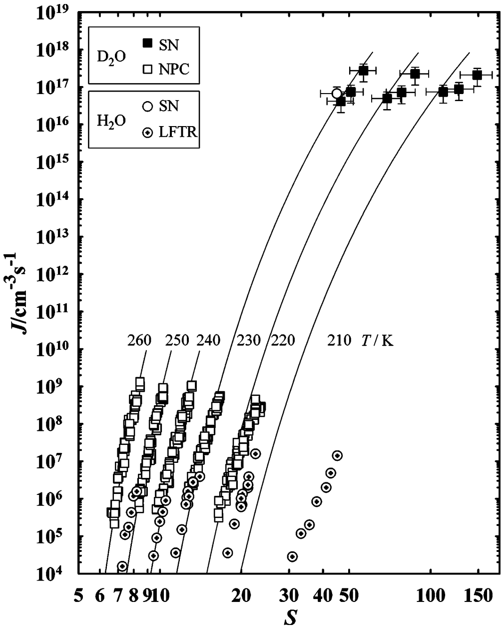

Figure 9. Nucleation rates of D_2O measured in the supersonic nozzles (SN) compared to those from the nucleation pulse chamber (NPC).[13] Solid lines are the predictions of the empirical function for the nucleation rate of D_2O from Wölk and Strey[13] (eq 20). The single H_2O nucleation rate measured in nozzle A is also shown, as are the H_2O nucleation rates measured by Mikheev et al.[8] in the laminar flow tube reactor (LFTR) On this plot, the H_2O nucleation rates from the nucleation pulse chamber would lie directly on top of the D_2O rates and are therefore omitted.

Figure 9 compares all of our D_2O data to the D_2O data of Wölk and Strey.[13] It also contains the data point corresponding to the single H_2O SANS experiment conducted as part of this study. The H_2O data of Mikheev[8] are also included because they overlap in temperature range with the current work as well as with that of Wölk and Strey.[13] The solid lines are calculated using the empirically corrected nucleation rate expression for D_2O developed by Wölk and Strey.[13] We can compare two isotopes of water directly because, as noted earlier, Wölk and Strey found that in the temperature range from 220−260 K the homogeneous nucleation rates of D_2O and H_2O agree within experimental error when the data are plotted as a function of the supersaturation.[13] The data of Mikheev et al.[8] for H_2O at 230, 240, and 250 K, measured in a laminar flow tube reactor (LFTR), confirm this observation, as does our single H_2O point. Furthermore, at 230 K all of the data agree quantitatively with the predictions of the empirical correlation across 13 orders of magnitude. At 220 K, the nozzle and nucleation pulse chamber rates both agree well with the empirical rate equation, and the LFTR data are shifted to higher S. Only at 210 K do the nozzle data also start move to higher S than the correlation, and even here the shift is not as dramatic as that observed by Mikheev et al. Finally, we note that although not shown here the rate predictions of Hale's scaled model[43,44] agree with all of the data in Figure 9 about as well as the empirical correlation does. Hale is preparing a detailed comparison of these results for publication soon.

The agreement between the data generated by very different experimental techniques, the empirical nucleation rate expression, and the scaled model of Hale[43,44] all support the view that although the supersaturation values reached in the nozzle are

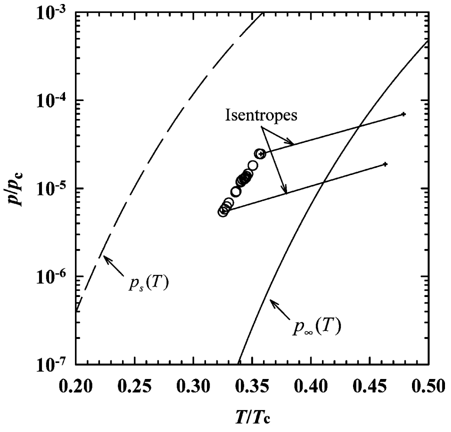

Figure 10. Pressure and temperature corresponding to the maximum nucleation rates in nozzle C (circles) compared to the equilibrium vapor pressure for D_2O, $p_\infty(T)$, and the vapor spinodal pressure, $p_s(T)$; p_c and T_c are the critical pressure and temperature, respectively. Because the location of the D_2O spinodal is not known, the curve shown was estimated by assuming that the pressure ratio $p_s(T/T_c)/p_\infty(T/T_c)$ for D_2O was equal to the corresponding ratio for the hard-sphere Yukawa fluid. The latter is easily determined from the mean-field equation of state.[45] The pressures corresponding to the maximum nucleation rate are well below those estimated for the spinodal, which is a strong indication that these experiments are not influenced by any effects that may occur close to the instability limit.

high the experiments are still not influenced by the spinodal. Quite simply, in an expansion device or a free expansion, high supersaturations are achieved by decreasing the equilibrium vapor pressure more rapidly than the vapor pressure of the condensable. As illustrated in Figure 10, in the temperature range of our experiments, the gas-phase pressure would have to be several orders of magnitude higher to be reach the estimated location of the spinodal. Even techniques such as free jets, with much higher expansion and cooling rates than our nozzles, are known[46] to produce low-density, nearly collisionless states distinctly different from conditions near the low-temperature spinodal.

E. Size and Excess Internal Energy of Critical Water Clusters. One of the goals of this research is to measure the properties of the critical clusters by applying the first and second nucleation theorems to the data. Figure 11a illustrates the fits to the current isothermal rate data from which we derived the experimental values of n^*. Strictly speaking, n^* is the *excess* number of molecules in the volume occupied by the critical cluster rather than the number of molecules in the critical cluster itself. At the equimolar dividing surface the ratio of the excess number to the number, however, equals $1 - (\rho_i/\rho_f)$ where ρ_i is the density of the initial phase and ρ_f is the density of the final phase. Under our operating conditions, (ρ_i/ρ_f) is approximately 10^{-6} and can safely be ignored.

In addition to the three rates measured (at each temperature) as part of this series of experiments, we have also included one point at each temperature from our earlier work.[23] In Figure 11b, the vertical error bars associated with the measured values of n^* correspond to the standard error of the slopes, and the horizontal error bars show the range in n^* predicted by the Gibbs−Thomson equation that stems from the uncertainty in S. In addition to the current data set, Figure 11b includes the critical cluster sizes measured by Wölk and Strey[13] for both isotopes of water and the values of n^* for H_2O that we derived from the data of Mikheev et al.[8] and Viisanen et al.[26,47] Almost all of the experimental values of n^* lie within ±20% of the predictions of the Gibbs−Thomson equation, including the low-temperature LFTR data that are at odds with the other rate measurements. Even when the critical cluster contains fewer than 10 molecules, only 1 point fails to meet this criterion.

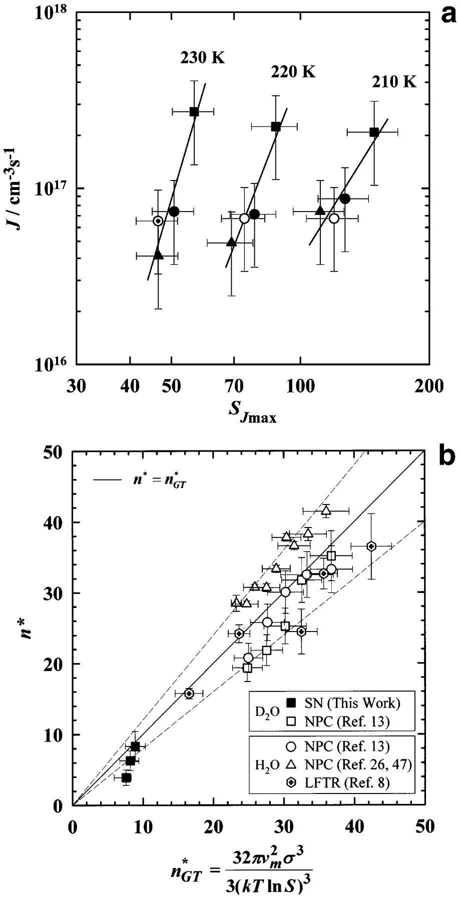

Figure 11. (a) Fits to the supersonic nozzle nucleation rate data used to derive n^*. The symbols used here correspond to those in Figure 8. (b) Values for n^* derived from the H_2O and D_2O data sets using eq 1 are in good agreement with the predictions of the Gibbs−Thomson equation, even when n^* is less than 10. The solid line corresponds to perfect agreement. Dashed lines correspond to the ±20% limits. Here, the symbols represent experimental data obtained from supersonic nozzles (SN), nucleation pulse chambers (NPC), and laminar flow tube reactors (LFTR).

We next applied the second nucleation theorem to the supersonic nozzle and nucleation pulse chamber data to calculate the excess internal energies of the clusters, $E_x(n^*)$. Physically, this quantity corresponds to the difference in the mean internal energy of the cluster and the energy that the n^* molecules would have, on average, if they were in the bulk liquid phase at the temperature and pressure of the vapor.[29]

For the supersonic nozzle, we first determined the average value of $\ln S_{J_{\max}}$ for each isothermal data set. We then used our correlations with mass flow rate to determine the corresponding values of $T_{J_{\max}}$ in each nozzle. Because the shifts in S and T are small, the value of the nucleation rate was not changed from the nearby measurement. As illustrated in Figure 12a, the data points corresponding to each data set including one point from Khan et al.[23] were fit to a straight line, and eq 2 was used to extract $E_x(n^*)$ from the measured slope. Following Ford's convention,[28,29] we normalized all of the energies by kT_0 with $T_0 = 273.15$ K.

For the Viisanen et al.[26,47] H_2O data, we followed the method outlined by Ford and evaluated

$$T\frac{\mathrm{d}(\ln S^{\mathrm{crit}})}{\mathrm{d}T} = -\frac{(E_x(n^*) + L - kT)}{kT(n^* + 1)} \qquad (21)$$

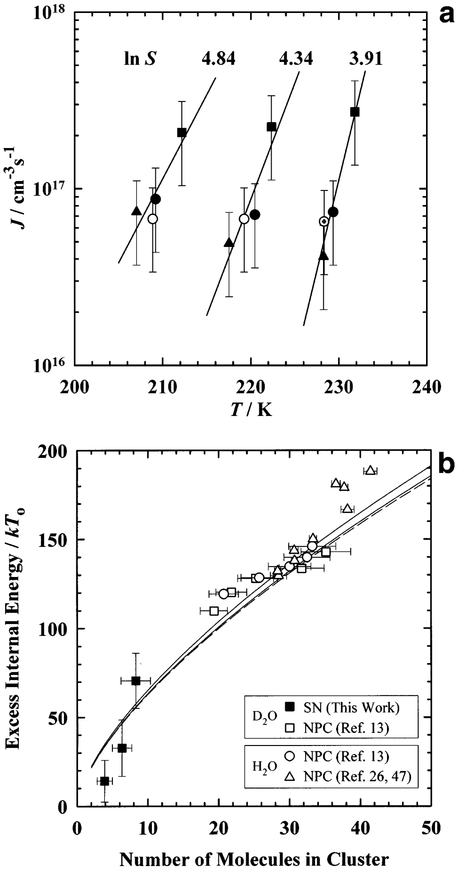

Figure 12. (a) Data used to derive $E_x(n^*)$ for the supersonic nozzle experiments. The symbols have the same meaning as those in Figure 8. (b) Excess internal energies of the critical clusters $E_x(n^*)$ plotted as a function of the number of molecules in the critical cluster. $T_0 = 273.15$ K. The lines are calculated using eq 23, and the solid lines correspond to eq 23 calculated for D_2O at 260 (upper line) and 210 K (lower line). The dashed line is for H_2O at 210 K. Abbreviations are the same as those for Figure 10b.

where the critical supersaturation S^{crit} corresponds to a nucleation rate of 10^7 cm^{-3} s^{-1}. We also attempted to reduce the Mikheev et al.[8] H_2O data this way using $J = 3 \times 10^5$ cm^{-3} s^{-1} as the critical nucleation rate, but the data are too sparse to analyze accurately.

Finally, for the Wölk and Strey[13] data we took advantage of the quantitative agreement between the experimental measurements and the empirically corrected nucleation rate expressions, eqs 19 and 20. Thus, for H_2O, $E_x(n^*)$ becomes

$$E_x(n^*) \cong kT^2\left(\frac{\mathrm{d}(\ln J_{H_2O})}{\mathrm{d}T}\right)_{\ln S} - L + kT \qquad (22)$$

where J_{H_2O} is given by eq 19. To evaluate eq 22, we determined the average value of ln S for each isothermal data set and substituted the values of ln S, T, and the corresponding values of n^* into our analytical expression for $[\mathrm{d}(\ln J_{H_2O})/\mathrm{d}T]_{\ln S}$. The same approach was used for the D_2O data.

Figure 12b summarizes the excess internal energies as a function of the critical cluster size. In the region of overlap, there is remarkably good agreement between the data sets generated in the nucleation pulse chamber. As the cluster size decreases into the regime covered by the supersonic nozzle, the data fall off much more rapidly. In the absence of intermediate experimental values, it is difficult to determine whether the data sets are consistent, and we therefore turn to theory to bridge the gap.

Within the framework of the capillarity approximation, Ford[28,29] showed that the excess internal energy of the critical cluster is given by

$$E_{xc}(n^*) = \left(\sigma - T\frac{\mathrm{d}\sigma}{\mathrm{d}T}\right)A_1(n^*)^{2/3} \qquad (23)$$

where $A_1(n^*)^{2/3}$ is the surface area of a spherical droplet containing n^* molecules. The upper and lower solid lines in Figure 12b correspond to eq 23 evaluated for D_2O at 260 and 210 K, respectively—the extreme temperature values for all of the experiments—and for the 50 degree change in temperature, the curves differ by only 3%. Equation 23 is quite insensitive to temperature even though the surface tension decreases with increasing temperature because this effect is largely offset by subtracting a term proportional to the surface tension derivative, itself a negative quantity. The long-dashed line corresponds to the 210 K line for H_2O, and as expected, there is little difference in the values of the excess internal energy predicted for the two isotopes of water. For clarity, we have not plotted the line corresponding to 260 K for H_2O. We note that we have extended eq 23 only down to $n^* = 2$. Applying this equation to a cluster smaller than the dimer does not make sense within the framework of classical nucleation theory. If the critical cluster is the monomer, then there is no barrier to the phase transition, and eq 23 is no longer relevant. Comparing the experimental data with the theoretical prediction, we find that most of the nucleation pulse chamber data agree quantitatively with the predictions of eq 23 and even the supersonic nozzle data are amazingly consistent.

Despite the astonishingly good agreement between the measured values of n^* and $E_x(n^*)$ presented here and those predicted by classical nucleation theory, we would like to interject a cautionary note. It is an empirical observation that near 240 K CNT does an amazing job of predicting the nucleation rates of both isotopes of water. As discussed in our earlier paper[48] in the temperature range from 220 to 260 K, most measured values of J_{exp} are within 2 orders of magnitude of J_{theory}. Furthermore, the Gibbs−Thomson equation has been found to hold very well for both water and for other substances such as the straight-chain alcohols[49,50] down to quite small cluster sizes. The challenge is to work with other substances or at other temperatures where CNT fails. Ford,[29] for example, found that the agreement between the predicted and measured values of $E_x(n^*)$ for hydrocarbons, n-pentanol, and n-nonane, for example, was far less good. More recently, preliminary onset measurements for Ar in a cryogenic nucleation pulse chamber[51,52] show that experimental nucleation rates are roughly 20 orders of magnitude higher than those predicted by classical nucleation theory. Given the scatter in the other existing Ar onset measurements, remeasuring the onset of Ar condensation in a supersonic nozzle is a crucial experiment. Together the two data sets are likely to yield values of n^* that are much smaller than those predicted by the Gibbs−Thomson equation, or as it will appear to the experimenter, the nucleation rate curves will be rather flat as a function of S. Preparations for such experiments are underway.

V. Conclusions

We have developed a method to measure isothermal homogeneous nucleation rates as a function of supersaturation in conventional Laval nozzles. A quantitative analysis of the pressure profiles shows that the condensation process produces a natural nucleation pulse that is ~10 μs long. Although the peak nucleation rate in a nozzle with a constant expansion rate does not vary much, we can measure significantly different rates by changing the expansion rate (i.e., by changing the opening angle of the nozzle). Higher expansion rates lead to deeper quenches into the metastable region and higher nucleation rates.

By independently controlling the stagnation temperature, the gas-phase composition, and the expansion rate of the supersonic nozzles, we can vary the peak supersaturation at a fixed temperature. Pressure profile measurements provide the characteristic nucleation time interval, Δt, and quantitative SANS measurements yield the droplet number density, N. Together these two quantities define the nucleation rate. In this way, we can generate isothermal nucleation rate curves and extend the accessible nucleation rate range by almost 10 orders of magnitude above those available in other measurement devices. Nevertheless, for both isotopes of water the nozzle data are consistent with a correction function to classical theory for water nucleation obtained from independent rate measurements in a nucleation pulse chamber where rates are many orders of magnitude lower.

The current data sets show that classical nucleation theory (CNT) quantitatively predicts the homogeneous nucleation of water at 240 K and the slope of the $J(S)$ curves over more than 10 orders of magnitude but slightly overpredicts the temperature dependence of the rates. Applying the first and second nucleation theorems to the data, we conclude that the number of molecules in the critical cluster n^* is correctly predicted by the Gibbs–Thomson equation and that the excess internal energy of the critical cluster is predicted very well by eq 23. The latter result implies that the poor temperature dependence of the classical rate theory for water is due mainly to its failure to treat the excess entropy of the critical cluster properly.[53] Although CNT is amazingly robust for water in this temperature range, for other molecules, even for the simple case of Ar, CNT can fail dramatically. Further progress depends both on measuring rates under less “favorable” conditions and on developing analysis methods that can pinpoint why the theory is failing.

Acknowledgment. This work was supported by the National Science Foundation under grant nos. CHE-0097896 and INT-0089897 and by the DAAD and by the Engineering Physics Program of the Division of Materials Sciences and Engineering, Basic Energy Sciences, U.S. Department of Energy. We acknowledge the support of the National Institute of Standards and Technology, U.S. Department of Commerce, in providing the facilities used in this work. We thank K. Iland, K. Streletzky, P. Paci, and J. Barker for their assistance during the SANS experiments. We thank S. Kline for support with the Igor Pro Procedures for the Doppler correction and for additional analysis programs. We thank I. Ford for suggesting that we evaluate the excess energy from the second nucleation theorem.

References and Notes

(1) Pound, G. M. *J. Phys. Chem. Ref. Data* **1972**, *1*, 119.
(2) Heist, R. H.; He, H. *J. Phys. Chem. Ref. Data* **1994**, *23*, 781.
(3) Katz, J. L.; Ostermier, B. J. *J. Chem. Phys*. **1967**, *47*, 478.
(4) Rudek, M. M.; Katz, J. L.; Uchtmann, H. *J. Chem. Phys*. **1999**, *110*, 11505.
(5) Heist, R. H.; Ahmed, J.; Janjua, M. *J. Phys. Chem*. **1994**, *98*, 4443.
(6) Hämeri, K.; Kulmala, M.; Krissinel, E.; Kodenyov, G. *J. Chem. Phys*. **1996**, *105*, 7683.
(7) Mikheev, V. B.; Laulainen, N. S.; Barlow, S. E.; Knott, M.; Ford, I. *J. Chem. Phys.* **2000**, *113*, 3704.
(8) Mikheev, V. B.; Irving, P. M.; Laulainen, N. S.; Barlow, S. E.; Pervukhin, V. V. *J. Chem. Phys*. **2002**, *116*, 10772.
(9) Adams, G. W.; Schmitt, J. L.; Zalabsky, R. A. *J. Chem. Phys*. **1984**, *81*, 5074.
(10) Lee, C. F. Condensation of H_2O and D_2O in Argon in the Centered Expansion Wave in a Shock Tube. In *Condensation in High-Speed Flows*; Pouring, A. A., Ed.; American Society of Mechanical Engineers: New York, 1977; pp 83–96.
(11) Peters, F.; Paikert, B. *Exp. Fluids* **1989**, *7*, 521.
(12) Strey, R.; Wagner, P. E.; Viisanen, Y. *J. Phys. Chem*. **1994**, *98*, 7748.
(13) Wölk, J.; Strey, R. *J. Phys. Chem. B* **2001**, *105*, 11683.
(14) Oswatitsch, K. *ZAMM* **1942**, *22*, 1.
(15) Hill, P. G. *J. Fluid. Mech*. **1966** *25*, 593.
(16) Stein, G. D.; Wegener, P. P. *J. Chem. Phys*. **1967**, *46*, 3685.
(17) Stein, G. D.; Moses, C. A. *J. Colloid Interface Sci*. **1972**, *39*, 504.
(18) Moses, C. A.; Stein, G. D. *J. Fluids Eng*. **1978**, *100*, 311.
(19) Pouring, A. A. Doctoral Dissertation, Yale University, New Haven, CT, 1963.
(20) Wegener, P. P.; Pouring, A. A. *Phys. Fluids* **1964**, *7*, 352.
(21) Wegener, P. P. *Acta Mechanica* **1975**, *21*, 65.
(22) Streletzky, K. A.; Zvinevich, Y.; Wyslouzil, B. E.; Strey, R. *J. Chem. Phys.* **2002**, *116*, 4058.
(23) Khan, A.; Heath, C. H.; Dieregsweiler, U. M.; Wyslouzil, B. E.; Strey, R. *J. Chem. Phys.* **2003**, *119*, 3138.
(24) Heath, C. H.; Streletzky, K. A.; Wyslouzil, B. E.; Wölk, J.; Strey, R. *J. Chem. Phys.* **2003**, *118*, 5465.
(25) Kashchiev, D. *J. Chem. Phys.* **1982**, *76*, 5098.
(26) Viisanen, Y.; Strey, R.; Reiss, H. *J. Chem. Phys.* **1993**, *99*, 4680.
(27) Oxtoby, D. W.; Kashchiev, D. *J. Chem. Phys.* **1994**, *100*, 7665.
(28) Ford, I. *J. Chem. Phys.* **1996**, *105*, 8324.
(29) Ford, I. *Phys. Rev. E* **1997**, *56*, 5615.
(30) Heath, C. H.; Streletzky, K.; Wyslouzil, B. E.; Wölk, J.; Strey, R. *J. Chem. Phys.* **2002**, *117*, 6176.
(31) Wyslouzil, B. E.; Heath, C. H.; Cheung, J. L.; Wilemski, G. *J. Chem. Phys.* **2000**, *113*, 7317.
(32) Dobbins, R. A. *J. Fluids Eng.* **1983**, *105*, 414.
(33) *NG3 and NG7 30-meter SANS Instruments Data Reduction Manual*; National Institute of Standards and Technology (NIST NCNR): Gaithersburg, MD, 2001; www.ncnr.nist.gov/programs/sans/manuals/data_red.html.
(34) Wilemski, G. *Phys. Rev. E* **2000**, *61*, 557.
(35) Wyslouzil, B. E.; Cheung, J. L.; Wilemski, G.; Strey, R.; Barker, J. *Phys. Rev. E* **1999**, *60*, 4330.
(36) Wyslouzil, B. E.; Cheung, J. L.; Wilemski, G.; Strey, R. *Phys. Rev. Lett.* **1997**, *79*, 431.
(37) *NG3 and NG7 30-meter SANS Instruments Data Analysis Manual*; National Institute of Standards and Technology (NIST NCNR): Gaithersburg, MD, 2001; www.ncnr.nist.gov/programs/sans/manuals/data_anal.html.
(38) Wagner, P. E.; Anisimov, M. *J. Aerosol Sci.* **1993**, *24*, S103.
(39) Becker, R.; Döring, W. *Ann. Phys.* (*Leipzig*) **1935**, *24*, 719.
(40) Wilemski, G. *J. Chem. Phys.* **1975**, *62*, 3772.
(41) Wyslouzil, B. E.; Wilemski, G. *J. Chem. Phys.* **1996**, *105*, 1090.
(42) Wilemski, G. In *Nucleation and Atmospheric Aerosols*; Fukuta, N., Wagner, P. E., Eds.; Deepak: Hampton, VA, 1992; p 71.
(43) Hale, B. N. *Phys. Rev. A* **1986**, *33*, 4156.
(44) Hale, B. N. *Metall. Trans. A* **1992**, *23*, 1863.
(45) Li, J.-S.; Wilemski, G. *J. Chem. Phys.* **2003**, *118*, 2845.
(46) Miller, D. R. In *Atomic and Molecular Beam Methods*; Scoles, G., Ed.; Oxford University: Oxford, U.K., 1988; Vol. 1, p 14.
(47) Viisanen, Y.; Strey, R.; Reiss, H. *J. Chem. Phys.* **2000**, *112*, 8205.
(48) Wölk, J.; Strey R.; Heath, C. H.; Wyslouzil, B. E. *J. Chem. Phys* **2002**, *117*, 4954.
(49) Strey, R.; Viisanen, Y.; Wagner, P. E. *J. Chem. Phys.* **1995**, *103*, 4333.
(50) Viisanen, Y.; Wagner, P. E.; Strey, R. *J. Chem. Phys.* **1997**, *108*, 4257.
(51) Fladerer, A.; Strey, R. *J. Aerosol Sci.* **2001**, *32*, S101–S102.
(52) Fladerer, A. Doctoral Dissertation, University of Cologne, Cologne, Germany, 2002.
(53) This inference is based on the assumption, as implied by the results of density functional theory,[54] that the poor temperature dependence is attributable primarily to the inadequacy of the classical free energy of cluster formation and not to the kinetic prefactor.
(54) Zeng, X. C.; Oxtoby, D. W. *J. Chem. Phys.* **1991**, *94*, 4472.